

Magnetic pyroxenes $\text{LiCrGe}_2\text{O}_6$ and $\text{LiCrSi}_2\text{O}_6$: dimensionality crossover in a non-frustrated $S = \frac{3}{2}$ Heisenberg model

O. Janson,^{1,2,*} G. Nénert,³ M. Isobe,⁴ Y. Skourski,⁵ Y. Ueda,⁴ H. Rosner,² and A. A. Tsirlin^{1,2}

¹*National Institute of Chemical Physics and Biophysics, 12618 Tallinn, Estonia*

²*Max-Planck-Institut für Chemische Physik fester Stoffe, Nöthnitzer Str. 40, 01187 Dresden, Germany*

³*Institut Laue Langevin, Grenoble 38042, France*

⁴*Institute for Solid State Physics, University of Tokyo, 5-1-5 Kashiwa, Chiba 277-8581, Japan*

⁵*Hochfeld-Magnetlabor Dresden, Helmholtz-Zentrum Dresden-Rossendorf, D-01314 Dresden, Germany*

(Dated: February 21, 2014)

The magnetism of magnetoelectric $S = \frac{3}{2}$ pyroxenes $\text{LiCrSi}_2\text{O}_6$ and $\text{LiCrGe}_2\text{O}_6$ is studied by density functional theory (DFT) calculations, quantum Monte Carlo (QMC) simulations, neutron diffraction, as well as low-field and high-field magnetization measurements. In contrast with earlier reports, we find that the two compounds feature remarkably different, albeit non-frustrated magnetic models. In $\text{LiCrSi}_2\text{O}_6$, two relevant exchange integrals, $J_1 \simeq 9$ K along the structural chains and $J_{\text{ic1}} \simeq 2$ K between the chains, form a 2D anisotropic honeycomb lattice. In contrast, the spin model of $\text{LiCrGe}_2\text{O}_6$ is constituted of three different exchange couplings. Surprisingly, the leading exchange $J_{\text{ic1}} \simeq 2.3$ K operates between the chains, while $J_1 \simeq 1.2$ K is about two times smaller. The additional interlayer coupling $J_{\text{ic2}} \simeq J_1$ renders this model 3D. QMC simulations reveal excellent agreement between our magnetic models and the available experimental data. Underlying mechanisms of the exchange couplings, magnetostructural correlations, as well as implications for other pyroxene systems are discussed.

PACS numbers: 75.50.Ee, 75.30.Et, 75.10.Jm, 75.60.Ej

I. INTRODUCTION

In the solid state, electricity and magnetism are related to two distinct primary order parameters and pertain to different spontaneously broken symmetries. The interplay of the two orders is ruled by the magnetoelectric (ME) coupling. The underlying mechanism is still debated,¹ yet a substantial progress is achieved in material-specific studies. Therefore, a viable way towards better understanding is to pick a certain class of ME compounds realizing different magnetic structures that would allow for a systematic study.

Pyroxenes are one of the most promising candidates for such a systematic study. This is a large group of natural minerals and inorganic compounds with a common chemical formula AMX_2O_6 , where the A site can be occupied by alkaline (Li and Na) or alkaline-earth (Mg and Ca) metals, the M site can accommodate various $3d$ transition metals, as well as Mg and Al. In natural pyroxenes, the X site is occupied by Si, while in most cases, the Ge counterpart can be synthesized.

Several pyroxene materials were recently shown to exhibit ME properties. For instance, the natural mineral acmite $\text{NaFeSi}_2\text{O}_6$ (Ref. 2) and its Ge-containing counterpart $\text{NaFeGe}_2\text{O}_6$ (Ref. 3) are ME multiferroics. ME effect was also observed in $\text{LiFeSi}_2\text{O}_6$,² as well as in Cr-based pyroxenes $\text{LiCrSi}_2\text{O}_6$ (Ref. 2) and $\text{LiCrGe}_2\text{O}_6$ (Ref. 4). To account for the ME properties of these materials, and facilitate the search for new ME pyroxenes, precise information on the magnetic model is essential.

The magnetism of pyroxenes is ruled by the M cations that form magnetic chains of edge-sharing MO_6 octahedra. Although these chains are common to all py-

roxenes, recent experiments reveal a variety of magnetic behaviors that can substantially deviate from the quasi-one-dimensional (1D) chain physics. For instance, the $S = 1/2$ compound $\text{CaCuGe}_2\text{O}_6$ is a spin dimer system.⁵ Another $S = 1/2$ compound, $\text{LiTiSi}_2\text{O}_6$, also has a singlet ground state (GS), but induced by orbital ordering.⁶ On the other hand, the $S = 1$ pyroxenes LiVGe_2O_6 (Ref. 7) and LiVSi_2O_6 (Ref. 8) exhibit long-range magnetic ordering, which is not expected in isolated or weakly coupled $S = 1$ chains showing Haldane physics.

The magnetic properties of pyroxenes are very sensitive to essentially nonmagnetic constituents of the crystal structure. An instructive example is given by $S = 3/2$ pyroxenes with magnetic $M = \text{Cr}^{3+}$ atoms. The title compounds, $\text{LiCrSi}_2\text{O}_6$ and $\text{LiCrGe}_2\text{O}_6$, feature the same type of antiferromagnetic order, albeit with different ordered magnetic moments.^{4,9} The magnetic structure of $\text{NaCrSi}_2\text{O}_6$ is similar to $\text{LiCrSi}_2\text{O}_6$ and $\text{LiCrGe}_2\text{O}_6$,⁴ but the value of the ordered magnetic moment ($2.3 \mu_B$) in $\text{NaCrSi}_2\text{O}_6$ indicates its resemblance to the $\text{LiCrGe}_2\text{O}_6$ germanate ($2.33 \mu_B$), not the $\text{LiCrSi}_2\text{O}_6$ silicate ($2.06 \mu_B$). However, its Ge counterpart, $\text{NaCrGe}_2\text{O}_6$, is a ferromagnet with the ordered moment of only $m_{\text{Cr}} = 1.85 \mu_B$, which is lower than in any other Cr^{3+} -based pyroxene compound.¹⁰

The variety of magnetic behaviors observed in pyroxenes is rooted in their electronic structure. Using perturbation theory and density functional theory (DFT) calculations, Streltsov and Khomskii studied the influence of the electronic state of the magnetic M cation (trivalent Ti, V, Cr, Mn, and Fe) and of the shortest distance between the neighboring in-chain M atoms on nearest-neighbor magnetic exchange J_1 .¹¹ However, the

intra-chain exchange J_1 alone does not suffice to account for the magnetic GS, which is influenced or even ruled by interchain couplings. Based on geometrical arguments, several authors alleged the presence of frustrated interchain couplings,^{4,11} yet no detailed investigation of the microscopic magnetic model was performed so far. The main obstacles of this task are the variety of possible superexchange paths and the low magnetic energy scale (several K) of the ensuing magnetic couplings. As a result, each pyroxene compound requires a careful evaluation of its pertinent microscopic parameters.

In this study, we perform a microscopic magnetic modeling for two ME pyroxenes, $\text{LiCrSi}_2\text{O}_6$ and $\text{LiCrGe}_2\text{O}_6$. They feature the same crystal and magnetic structure, yet substantially different Curie-Weiss temperatures ($\theta = 34$ K and 6.5 K in $\text{LiCrSi}_2\text{O}_6$ and $\text{LiCrGe}_2\text{O}_6$, respectively) and magnetic ordering temperatures ($T_N = 11.1$ K and $T_N = 4.8$ K). Moreover, $\text{LiCrSi}_2\text{O}_6$ shows a broad maximum in the magnetic susceptibility at low temperatures, typical for the low-dimensional magnetism, while the $\text{LiCrGe}_2\text{O}_6$ closely resembles a three-dimensional antiferromagnet. Finally, in the magnetically ordered GS, local magnetic moments are notably different: $2.06(4)$ and $2.33(3) \mu_B/\text{Cr}$ in $\text{LiCrSi}_2\text{O}_6$ and $\text{LiCrGe}_2\text{O}_6$, respectively.^{4,9}

To elucidate the origin of the different magnetic behaviors, we use a combination of DFT calculations, quantum Monte Carlo (QMC) simulations, as well as experimental neutron diffraction and high-field magnetization measurements. We find that the magnetic properties of $\text{LiCrSi}_2\text{O}_6$ are described by an $S = 3/2$ (isotropic) Heisenberg model on a 2D anisotropic honeycomb lattice. The two leading exchanges are $J_1 \simeq 9$ K along the structural chains and $J_{ic1} \simeq 2$ K operating via double bridges of SiO_4 tetrahedra between the chains. By contrast, $\text{LiCrGe}_2\text{O}_6$ features, in addition to J_1 and J_{ic1} , another interchain coupling J_{ic2} , also operating along the double bridges of GeO_4 tetrahedra. The $J_1 : J_{ic1} : J_{ic2} = 0.5 : 1 : 0.5$ ratio according to our investigations indicates a 3D magnetism, with the leading interchain coupling $J_{ic1} \simeq 2.3$ K. Extensive QMC simulations for both microscopic models reveal excellent agreement with all available experimental data, including the hitherto never reported high-field magnetization curves.

This paper is organized as follows. Sec. II contains information on methodological and technical aspects of our DFT and QMC studies, as well as neutron diffraction and magnetization measurements. The crystal structure of pyroxenes is briefly discussed in Sec. III. Microscopic DFT-based modeling, QMC simulations of the resulting model and comparison with the experiments are presented in Sec. IV. The ordered magnetic moment, the mechanisms facilitating in-chain and interchain couplings, as well as magnetostructural correlations are discussed in Sec. V. Finally, the results are summarized in Sec. VI.

II. METHODS

Polycrystalline samples of $\text{LiCrSi}_2\text{O}_6$ and $\text{LiCrGe}_2\text{O}_6$ were prepared by a solid-state reaction with an appropriate molar ratio of Li_2CO_3 , Cr_2O_3 , and GeO_2 (SiO_2). The weighted mixtures were pressed into pellets and heated at 1273 K in air for several days with one intermediate grinding.

Neutron-diffraction measurements were carried out on powder samples. The stoichiometry of the compounds as well as their precise crystal structures were investigated using high resolution powder data at 1.8 K using the D2B diffractometer at the Institut Laue Langevin. The measurements were carried out at a wavelength of 1.594 Å corresponding to the (335) Bragg reflexion of a germanium monochromator. The neutron detection is performed with ^3He counting tubes spaced at 1.25° intervals. A complete diffraction pattern (Fig. 1) is obtained after about 25 steps of 0.05° in 2θ .

Magnetic susceptibility was measured in a SQUID MPMS magnetometer in the temperature range 1.8 – 380 K in applied fields of 0.1 – 5 T. High-field magnetization curves were measured on powder samples at a constant temperature of 1.5 K using a pulsed magnet at the Dresden High Magnetic Field Laboratory (HLD), as described in Ref. 12.

DFT calculations were performed using two different codes: the full-potential code FPLO9.03-37 (Ref. 13), as well as the pseudopotential code VASP-5.2 (Ref. 14). For the exchange and correlation potentials, we used both local density approximation¹⁵ (LDA) and generalized gradient approximation¹⁶ (GGA). Strong electronic correlations were treated in the DFT+ U scheme. Alternatively, we used the hybrid functionals PBE0 (Ref. 17) and HSE06 (Ref. 18) containing a fraction of the exact (Hartree-Fock) exchange. For VASP-5.2 calculations, we used the default projector-augmented wave (“PAW-PBE”) pseudopotentials. For the DFT+ U calculations, the fully localized limit (FLL) flavor of the double-counting correction was used. The on-site repulsion and Hund’s exchange were fixed at $U_{3d} = 3$ eV and $J_{3d} = 1$ eV.¹⁹

The experimental lattice constants and atomic coordinates were used as a structural input.²⁰ For non-magnetic calculations, \vec{k} -meshes of $16 \times 16 \times 12$ points (882 points in the irreducible wedge) were used. Wannier functions (WF) for the Cr $3d$ states were evaluated using the procedure described in Ref. 21. Spin-polarized calculations were performed for magnetic supercells of two types: (i) symmetry-reduced (space group $P1$) supercells, metrically equivalent to the crystallographic unit cells ($6 \times 6 \times 4$ \vec{k} -points), and (ii) symmetry-reduced (space group $P1$) supercells doubled along the c axis ($2 \times 2 \times 2$ \vec{k} -points).

QMC simulations were performed using the codes LOOP (Ref. 22) and DIRLOOP_SSE (Ref. 23) from the software package ALPS-2.1.1.²⁴ All simulations were performed on finite lattices using periodic boundary condi-

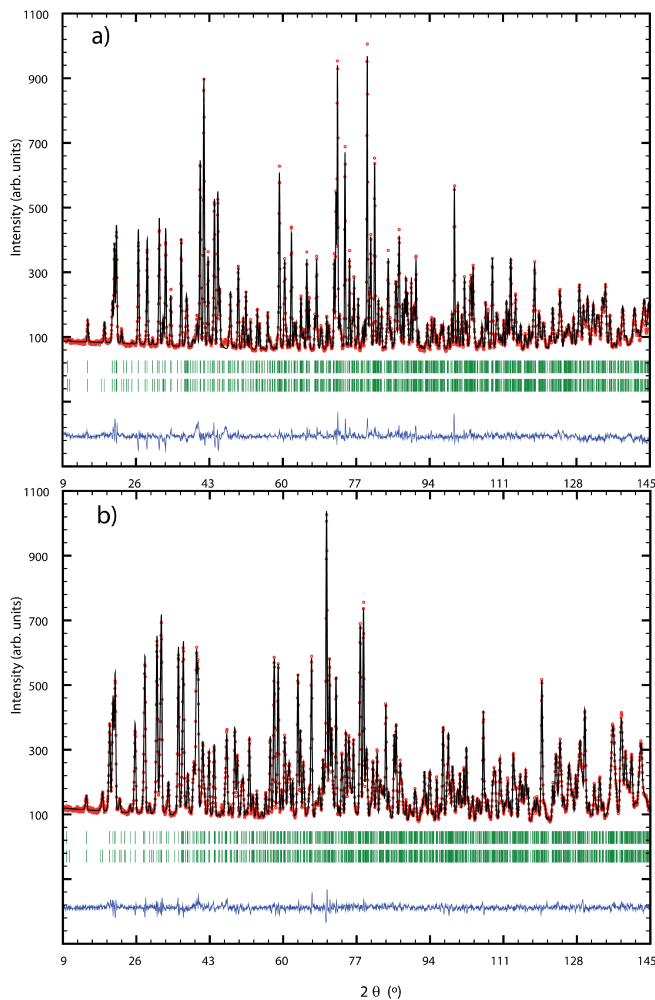


FIG. 1. (Color online) Neutron powder pattern ($\lambda = 1.594 \text{ \AA}$) of $\text{LiCrSi}_2\text{O}_6$ (a) and $\text{LiCrGe}_2\text{O}_6$ (b) collected at 1.8 K using the D2B diffractometer. The refinement has been done in the $P2_1/c$ (14) space group with the following statistics: $R_p = 4.55\%$ and $R_{wp} = 5.97\%$ for $\text{LiCrSi}_2\text{O}_6$ and $R_p = 4.55\%$ and $R_{wp} = 1.97\%$ for $\text{LiCrGe}_2\text{O}_6$.

tions. Temperature dependencies of the magnetic susceptibility were simulated on finite lattices of 1152 and 864 $S = 3/2$ spins for $\text{LiCrSi}_2\text{O}_6$ and $\text{LiCrGe}_2\text{O}_6$, respectively. To simulate the magnetization process, finite lattices of 288 ($\text{LiCrSi}_2\text{O}_6$) and 2048 ($\text{LiCrGe}_2\text{O}_6$) spins were used. The magnetic ordering transition temperature was estimated as the intersection of $N\rho_S(T)$ curves computed for different finite lattices, where ρ_S is the spin stiffness and N is the size of the finite lattice. The static structure factor \mathbb{S} was simulated on finite lattices of up to 1024 spins.

III. CRYSTAL STRUCTURE

Two different monoclinic modifications of $\text{LiCrSi}_2\text{O}_6$ are known. The high-temperature phase crystallizes in

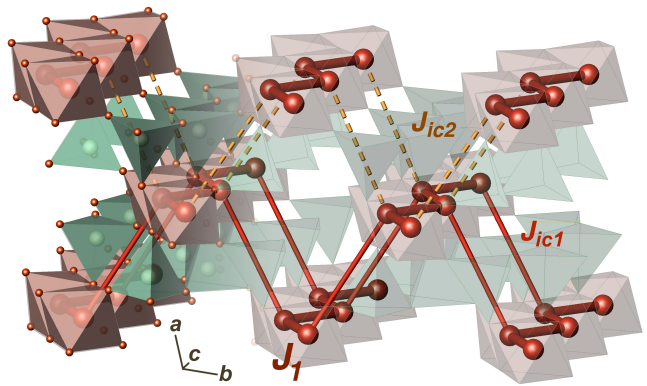


FIG. 2. (Color online) Crystal structure and magnetic model of LiCrX_2O_6 ($X = \text{Si, Ge}$). The crystal structure is formed by chains of edge-sharing CrO_6 octahedra (Cr atoms shown as large spheres) and chains of corner-sharing SiO_4 tetrahedra running along c . The spin model features the nearest-neighbor coupling J_1 (thick solid lines) along the structural chains, as well as two interchain couplings J_{ic1} (thin solid lines) and J_{ic2} (dashed lines). Note that J_1 and J_{ic1} form a 2D anisotropic honeycomb lattice.

the base-centered monoclinic space group $C2/c$.²⁵ Below 330 K, it transforms into the low-temperature phase with the reduced symmetry (sp. gr. $P2_1/c$);^{9,25} the differences between the two modifications are extensively discussed in Ref. 25. For $\text{LiCrGe}_2\text{O}_6$, the situation is more involved. The low-temperature modification is $P2_1/c$,⁴ but room-temperature measurements are controversial: the authors of Ref. 26 refined their x-ray diffraction data in the primitive space group, while Ref. 27 reports the base-centered space group based on synchrotron measurements. Investigation of the phase stability at room temperature is beyond the scope of the present study, hence we restrict ourselves to the low-temperature $P2_1/c$ phases of $\text{LiCrSi}_2\text{O}_6$ and $\text{LiCrGe}_2\text{O}_6$.

The structure of the low-temperature modification is shown in Fig. 2. It is shaped by alteration of two chain-like elements: (i) cationic chains of edge-sharing CrO_6 octahedra and (ii) anionic chains of corner-sharing XO_4 tetrahedra, both running along the crystallographic c axis. The symmetry reduction toward $P2_1/c$ is essential for the magnetic properties: it gives rise to inequivalent interchain couplings, in particular J_{ic1} and J_{ic2} depicted in Fig. 2.

As will be shown below, the magnetic properties of LiCrX_2O_6 ($X = \text{Si, Ge}$) depend on subtle structural details. Therefore, for a microscopic DFT-based analysis, reliable crystallographic information is a prerequisite. Here, we use neutron powder diffraction to determine the low-temperature crystal structures for both compounds. The resulting unit cell parameters and atomic coordinates are provided in Table. I.

TABLE I. Atomic coordinates and isotropic displacement parameters U_{iso} (in 10^{-2} \AA^2) determined by neutron powder diffraction ($\lambda = 1.594 \text{ \AA}$) at 2 K. The space group is $P2_1/c(14)$. The unit cell parameters are $a = 9.7919(1) \text{ \AA}$, $b = 8.7149(1) \text{ \AA}$, $c = 5.33461(6) \text{ \AA}$, $\beta = 108.9146(6)^\circ$ for $\text{LiCrGe}_2\text{O}_6$ and $a = 9.5122(4) \text{ \AA}$, $b = 8.5713(4) \text{ \AA}$, $c = 5.2229(2) \text{ \AA}$, $\beta = 109.7569(7)^\circ$ for $\text{LiCrSi}_2\text{O}_6$. All atoms occupy the $4e$ Wyckoff positions.

$\text{LiCrGe}_2\text{O}_6$				
Atom	x/a	y/b	z/c	U_{iso}
Li	0.2579(7)	0.0138(6)	0.2184(12)	0.62(11)
Cr	0.2515(3)	0.6593(4)	0.2118(6)	0.39(5)
Ge1	0.04756(14)	0.34430(17)	0.2750(3)	0.38(2)
Ge2	0.55472(13)	0.84153(19)	0.2294(2)	0.38(2)
O1a	0.85755(19)	0.3326(3)	0.1740(3)	0.50(2)
O1b	0.36416(19)	0.8316(3)	0.1043(4)	0.50(2)
O2a	0.11481(20)	0.5264(2)	0.2840(4)	0.50(2)
O2b	0.6312(2)	0.0065(2)	0.3874(4)	0.50(2)
O3a	0.11786(19)	0.29075(20)	0.6099(4)	0.50(2)
O3b	0.6136(2)	0.6879(2)	0.4544(4)	0.50(2)
$\text{LiCrSi}_2\text{O}_6$				
Atom	x/a	y/b	z/c	U_{iso}
Li	0.2517(10)	0.0120(7)	0.2280(17)	0.77(13)
Cr	0.2516(5)	0.6579(5)	0.2351(8)	0.62(6)
Si1	0.0497(3)	0.3412(4)	0.2729(6)	0.26(6)
Si2	0.5501(4)	0.8409(4)	0.2485(6)	0.40(6)
O1a	0.8668(3)	0.3325(3)	0.1660(5)	0.54(5)
O1b	0.3668(3)	0.8355(3)	0.1290(5)	0.74(5)
O2a	0.1171(3)	0.5116(3)	0.3066(5)	0.65(5)
O2b	0.6252(3)	0.0056(3)	0.3561(5)	0.44(5)
O3a	0.1100(3)	0.2692(3)	0.5835(5)	0.53(4)
O3b	0.6069(3)	0.7171(3)	0.5000(5)	0.55(5)

IV. MICROSCOPIC MAGNETIC MODELING

A. DFT calculations

We start our analysis with nonmagnetic band structure calculations. The density of states (DOS) in both $\text{LiCrSi}_2\text{O}_6$ and $\text{LiCrGe}_2\text{O}_6$ indicates the $3d^3$ configuration of Cr^{3+} : the valence band comprises the half-filled t_{2g} and the empty e_g manifold, split by the crystal field (Fig. 3). As expected for an octahedral coordination, the e_g orbitals are mixed with O $2p$ states, while the bands at the Fermi level are almost pure Cr t_{2g} states. The sizable exchange splitting, typical for Cr^{3+} , splits the t_{2g} manifold into well-separated spin up and spin down densities and ensures the high-spin configuration, readily obtained in spin-polarized calculations.

The magnetism of Cr^{3+} pyroxenes is driven by two concurrent processes: the AF exchange ensuing from the hopping between the half-filled t_{2g} orbitals, and the FM exchange due to the hopping between half-filled t_{2g} to the

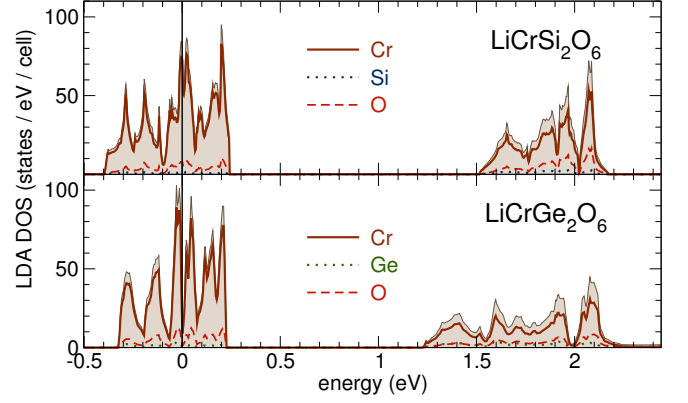


FIG. 3. (Color online) Nonmagnetic LDA total and atomic-resolved density of states (DOS) for $\text{LiCrSi}_2\text{O}_6$ and $\text{LiCrGe}_2\text{O}_6$. The Fermi level is at zero energy. GGA yields an almost indistinguishable DOS.

empty e_g orbitals.¹¹ To estimate the hopping integrals between different d orbitals of Cr, we construct Wannier functions and evaluate the on-site energies and transfer integrals as diagonal and non-diagonal elements, respectively. For both compounds, we find only three paths that substantially contribute to the electron transfer. In accord with the previous DFT studies,¹¹ the dominant coupling t_1 operates along the structural chains. Two other couplings, $t_{\text{ic}1}$ and $t_{\text{ic}2}$, are long-range and operate via double bridges of GeO_4 or SiO_4 tetrahedra. The full hopping matrices for these couplings are provided in Supplementary information.²⁰

Comparison of different hopping processes allows us to perform a qualitative analysis and estimate the leading exchange couplings. We start with the nearest-neighbor exchange J_1 . In $\text{LiCrSi}_2\text{O}_6$, the strongest hoppings within the t_{2g} manifold occurs between the yz and the xz orbital of the neighboring Cr atom (135 meV). The ensuing strong AF exchange is balanced by a sizable hopping to the empty $x^2 - y^2$ orbital (140 meV), which contributes to the FM exchange. The situation in $\text{LiCrGe}_2\text{O}_6$ is different: here, the strongest hopping occurs between the xz and the e_g orbitals, while the hoppings within the t_{2g} manifold are suppressed (< 100 meV). This difference is responsible for the suppression of J_1 in the Ge system.

The interchain coupling is realized along the two inequivalent paths, involving double bridges of anionic tetrahedra. Each of the interchain couplings $t_{\text{ic}1}$ and $t_{\text{ic}2}$ is dominated by a single matrix element from the t_{2g} manifold amounting to 60–70 meV, and two sizable hoppings between the t_{2g} and e_g states. The small energy scale of these concurrent processes impedes a reliable estimation of the resulting exchange. For a more robust, although still qualitative estimate, we turn to total energy DFT+ U and hybrid functional calculations.

A well-known drawback of conventional DFT approaches (LDA and GGA) is a severe underestimation of

electronic correlations within the $3d$ shell of Cr^{3+} , leading to underestimated band gaps²⁸ and overestimated exchange integrals.¹⁹ The simplest, yet widely renowned approach to mend this problem is the DFT+ U method, which accounts for the correlations by treating the on-site Coulomb repulsion U_d and the on-site Hund's exchange J_d between the d electrons in a mean-field fashion.

Here, we adopt $U_d = 3.0$ eV and $J_d = 1.0$ eV that accurately reproduce the experimental magnetic behavior for the recently studied quasi-1D compound $\text{Cr}_2\text{BP}_3\text{O}_{12}$,¹⁹ and apply both LSDA+ U and GGA+ U functionals. The resulting values are given in Table II. Both functionals yield similar values for the interchain coupling, but the J_1 estimates are remarkably different, especially for $\text{LiCrGe}_2\text{O}_6$. Since there are no *a priori* arguments favoring one of the functionals, we additionally use an independent computational method.

Recent studies render hybrid functionals (HF) as a feasible alternative to DFT+ U calculations.²⁹ This method restores the insulating GS by admixing the Fock exchange into the standard DFT exchange and correlation potential. There is an empirical evidence that the resulting total energies can provide accurate estimates for the magnetic exchanges.³⁰ Here, we use the PBE0 (Ref. 17) and HSE06 (Ref. 18) functionals that are particularly suited for inorganic compounds, and involve only one free parameter β , which controls the mixing between DFT and the Fock exchange. To provide unbiased results, we fix this parameter to the empirically determined optimal value $\beta = 0.25$.³¹ The resulting exchange values are given in Table II.

Despite the low energy scale of magnetic couplings in both compounds, the comparison of results obtained using different methods is quite instructive. First, the difference between different HF schemes, PBE0 and HSE06, is marginal, in line with previous studies.³² Second, we can directly compare the HF results with DFT+ U . For $\text{LiCrSi}_2\text{O}_6$, HF and GGA+ U yield similar results, while LSDA+ U finds a substantially smaller J_1 (Table II). The $\text{LiCrGe}_2\text{O}_6$ case is more involved. Here, the HF estimates are ~ 1.5 K smaller, than in GGA+ U . This difference is particularly important for J_1 : LSDA+ U and HF yield FM exchange, in contrast with a small AF exchange in GGA+ U . Fortunately, the sign of J_1 can be readily determined from the experimental magnetic structure, because the J_1 - J_{ic1} - J_{ic2} model is not frustrated. Thus, the mutual arrangement of neighboring magnetic moments in the spin chains is solely ruled by the sign of J_1 : parallel for FM J_1 , and antiparallel for AF J_1 . Since the neighboring Cr moments are antiparallel in the spin chains of both compounds,^{4,9} the solutions with FM J_1 can be ruled out.

Regarding the interchain couplings, we note that both J_{ic1} and J_{ic2} couple the chains antiferromagnetically. As the pathways of these interactions involve an additional shift along c (Fig. 2), the periodicities of the crystallographic and magnetic unit cells match (the propagation vector is $\mathbf{k} = 0$). On the phenomenological level, this

TABLE II. Leading exchange integrals (in K) in $\text{LiCrSi}_2\text{O}_6$ and $\text{LiCrGe}_2\text{O}_6$ as yielded by DFT+ U (LSDA+ U , GGA+ U) and hybrid-functional (PBE0, HSE06) calculations. For the latter, resolving J_{ic1} and J_{ic2} was computationally unfeasible. The minus sign indicates that the respective exchange coupling is FM.

LiCrSi ₂ O ₆			
	J_1	J_{ic1}	J_{ic2}
LSDA+ U (FLL, $U_d = 3$ eV)	5.3	3.7	1.0
GGA+ U (FLL, $U_d = 3$ eV)	10.4	3.0	1.0
PBE0	11.1	$\Sigma = 3.7$	
HSE06	11.6	$\Sigma = 3.6$	
LiCrGe ₂ O ₆			
	J_1	J_{ic1}	J_{ic2}
LSDA+ U (FLL, $U_d = 3$ eV)	-4.1	4.5	0.7
GGA+ U (FLL, $U_d = 3$ eV)	1.1	3.6	0.9
PBE0	-0.5	$\Sigma = 2.9$	
HSE06	-0.8	$\Sigma = 2.9$	

readily yields an effective FM interchain coupling, as indeed suggested in the earlier studies.^{4,9,10} Yet, it should be kept in mind that this FM “coupling” results from two *microscopic* AF exchanges J_{ic1} and J_{ic2} .

Despite the same topology of the spin lattice, the magnetic properties of $\text{LiCrSi}_2\text{O}_6$ and $\text{LiCrGe}_2\text{O}_6$ are remarkably different. The silicate system shows a distinct hierarchy of the magnetic exchange couplings: $J_1 \gg J_{\text{ic1}} \gg J_{\text{ic2}}$. The dominance of the in-chain coupling J_1 renders this compound as magnetically quasi-1D. In contrast, a substantial reduction of J_1 in $\text{LiCrGe}_2\text{O}_6$ leads to a physically different regime, where the interchain coupling J_{ic1} overtakes the leading role. Thus, the effective magnetic dimensionality of $\text{LiCrGe}_2\text{O}_6$ is quasi-3D.

B. Model simulations

DFT calculations provide a microscopic insight into the nature of the leading couplings, yet the numerical accuracy does not suffice to deliver an accurate quantitative spin model. In the following, we adopt the DFT-based microscopic magnetic models and refine the model parameters by simulating the experimentally observed quantities: temperature dependence of the magnetic susceptibility, field dependence of the magnetization, and the ordered magnetic moment.

In $\text{LiCrSi}_2\text{O}_6$, the interplane coupling J_{ic2} is much smaller than J_{ic1} , thus it can be neglected in a minimal model. To fit the experimental magnetic susceptibility of $\text{LiCrSi}_2\text{O}_6$, we perform QMC simulations of the 2D J_1 - J_{ic1} model, adopting $J_{\text{ic1}}:J_1 \simeq 0.25$ from GGA+ U and HF calculations (Table II). We obtain an excellent fit (Fig. 4) with $J_1 = 9.0$ K, the g -factor

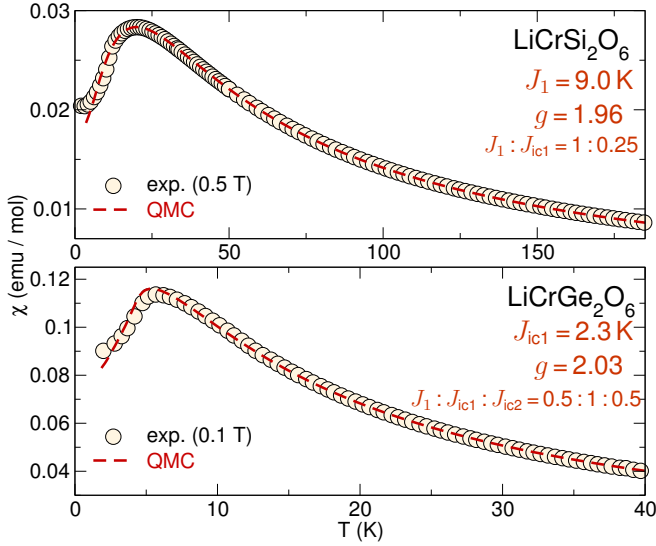


FIG. 4. (Color online) QMC fits (dashed line) to the experimental magnetic susceptibilities (symbols) of $\text{LiCrSi}_2\text{O}_6$ (top) and $\text{LiCrGe}_2\text{O}_6$ (bottom) measured in field of 0.5 T and 0.1 T, respectively. Note that the temperature scale is different in both panels. The leading magnetic exchange coupling amounts to $J_1 = 9.0$ K in $\text{LiCrSi}_2\text{O}_6$ and $J_{ic1} = 2.2$ K in $\text{LiCrGe}_2\text{O}_6$. The ratios of the exchange couplings amount to $J_1 : J_{ic1} = 1 : 0.25$ for $\text{LiCrSi}_2\text{O}_6$ and $J_1 : J_{ic1} : J_{ic2} = 0.5 : 1 : 0.5$ for $\text{LiCrGe}_2\text{O}_6$, respectively. The temperature-independent contribution χ_0 amounts to 7.9×10^{-5} emu/mol and -4.4×10^{-4} emu/mol in $\text{LiCrSi}_2\text{O}_6$ and $\text{LiCrGe}_2\text{O}_6$.

of 1.96, and the temperature-independent contribution $\chi_0 = 7.9 \times 10^{-5}$ emu/mol.

The magnetic model of $\text{LiCrGe}_2\text{O}_6$ is very different. First, the $|J_1|/J_{ic1}$ ratio is substantially smaller than in $\text{LiCrSi}_2\text{O}_6$. Second, the interchain coupling J_{ic2} , inactive in $\text{LiCrSi}_2\text{O}_6$, is of the order of J_1 and can not be neglected. DFT calculations suggest that the leading coupling is J_{ic1} , yet the estimates for J_1 are not accurate enough to decide on the value and even on the sign of the intrachain coupling. To refine the values of exchange integrals, we studied a wide range of J_1/J_{ic1} and J_{ic2}/J_{ic1} ratios, searching for the best possible agreement with the experimental $\chi(T)$ and the magnetic ordering temperature. In this way, we find that $J_1 : J_{ic1} : J_{ic2} = 0.5 : 1 : 0.5$ with $J_{ic1} = 2.3$ K and the g -factor of 2.03, supplied with the temperature-independent contribution $\chi_0 = -4.4 \times 10^{-4}$ emu/mol provide a good fit for the $\chi(T)$ data above the magnetic ordering temperature (see Fig. 4), and reasonably agree with the latter ($T_N = 4.2$ K versus the experimentally observed 4.8 K).

Despite the good agreement, we can not exclude that other solutions may provide an equally good description of the experimental data. In general, fits to the $\chi(T)$ data are prone to ambiguous solutions, since the magnetic susceptibility yields information on the momentum-integrated and thermally-averaged magnetic excitation spectrum. For simple systems, such as spin dimers or

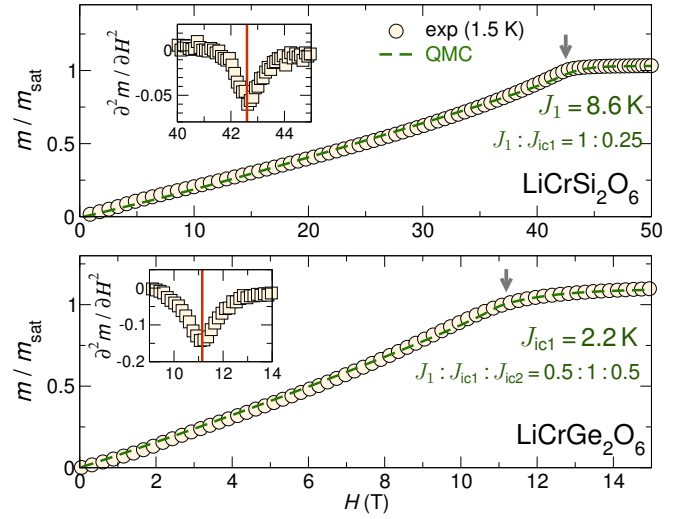


FIG. 5. (Color online) Magnetization curves (circles) of $\text{LiCrSi}_2\text{O}_6$ (top) and $\text{LiCrGe}_2\text{O}_6$ (bottom) measured in a pulsed magnetic field at 1.5 K. Note the different scales for the applied field in both panels. Solid lines are QMC simulations of the 2D anisotropic honeycomb lattice (J_1 - J_{ic1}) model for $\text{LiCrSi}_2\text{O}_6$ and the 3D J_1 - J_{ic1} - J_{ic2} model for $\text{LiCrGe}_2\text{O}_6$. The ratios of the exchange couplings amount to $J_1 : J_{ic1} = 1 : 0.25$ and $J_1 : J_{ic1} : J_{ic2} = 0.5 : 1 : 0.5$ for $\text{LiCrSi}_2\text{O}_6$ and $\text{LiCrGe}_2\text{O}_6$, respectively. The m_{sat} is the value of magnetization at the saturation field, which is defined as a local minimum of the second derivative (insets).

chains, this information suffices to evaluate the single relevant model parameter. For more complicated systems featuring several relevant exchange couplings, $\chi(T)$ generally allows for ambiguous solutions.³³ Additional information from an independent experiment is vital to resolve this problem. Therefore, we perform high-field magnetization measurements that are particularly sensitive to the structure of the magnetic excitation spectrum. The low energy scale of magnetic couplings in $\text{LiCrSi}_2\text{O}_6$ and especially $\text{LiCrGe}_2\text{O}_6$ allowed us to reach saturation in a standard pulsed-field experiment.

Magnetization curves for $\text{LiCrSi}_2\text{O}_6$ and $\text{LiCrGe}_2\text{O}_6$ are shown in Fig. 5.³⁴ The transition to the fully polarized state (saturation) can be traced as a local minimum in the second derivative of magnetization (Fig. 5, insets). The different magnetic energy scales in $\text{LiCrSi}_2\text{O}_6$ and $\text{LiCrGe}_2\text{O}_6$ ensue very different saturation fields: 42.5 T and 11.2 T, respectively.

We simulate the $M(H)$ dependence using QMC and scale the simulated curves using the g -factor values from the $\chi(T)$ fits (1.96 and 2.03 for $\text{LiCrSi}_2\text{O}_6$ and $\text{LiCrGe}_2\text{O}_6$, respectively). The reduced temperature $T/\max\{J, J_{ic1}\}$ is chosen to match the experimental measurement temperature, which was ~ 1.5 K in both cases. Therefore, the only adjustable parameter of the fit is the energy scale $\max\{J_1, J_{ic1}\}$, which is varied in order to get the best agreement with the experimental curve.

In this way, we find that the $J_1 : J_{ic1} = 1 : 0.25$ solution with $J_1 = 8.6$ K yields good agreement with the experimental magnetization isotherm of $\text{LiCrSi}_2\text{O}_6$ (Fig. 5), justifying our restriction to the 2D J_1 - J_{ic1} model. For $\text{LiCrGe}_2\text{O}_6$, we also obtain an excellent agreement for the 3D model with $J_1 : J_{ic1} : J_{ic2} = 0.5 : 1 : 0.5$ and $J_{ic1} = 2.3$ K (Fig. 5). Again, QMC simulations to the $M(H)$ behavior fully support the model assignment based on DFT calculations and $\chi(T)$ fits.

V. DISCUSSION

DFT calculations reveal a substantial difference between the magnetism of $\text{LiCrSi}_2\text{O}_6$ and $\text{LiCrGe}_2\text{O}_6$. The spin model of the former features two relevant exchange couplings, J_1 and J_{ic1} , topologically equivalent to a honeycomb lattice (Fig. 6). $\text{LiCrSi}_2\text{O}_6$ is in the quasi-1D limit of this model ($J_1 \gg J_{ic1}$), corroborated experimentally by the broad maximum in $\chi(T)$. In contrast, the spin model of $\text{LiCrGe}_2\text{O}_6$ comprises three relevant exchange couplings: J_1 and J_{ic1} , as in $\text{LiCrSi}_2\text{O}_6$, as well as the additional coupling J_{ic2} . The ratios $J_1 : J_{ic1} : J_{ic2}$ are close to $0.5 : 1 : 0.5$, thus the resulting model is 3D.

A. Ordered magnetic moment

One of the main objectives of our study is to elucidate the microscopic origin for the difference between the ordered magnetic moments on Cr atoms: $2.06 \mu_B$ in $\text{LiCrSi}_2\text{O}_6$ and $2.33 \mu_B$ in $\text{LiCrGe}_2\text{O}_6$.^{4,9} For a given spin lattice, the magnetic moment can be estimated from the respective static structure factor \mathbb{S} simulated on finite lattices. The ordered magnetic moment is related to \mathbb{S} and the finite lattice size N :

$$m(N) = \sqrt{\frac{3\mathbb{S}}{N}} \quad (1)$$

For the finite-size scaling, we use the expression based on Eq. (39b) of Ref. 35:

$$m = \sqrt{m(N) - \frac{m_1}{\sqrt{N}} - \frac{m_2}{N}} \quad (2)$$

We first start with the 2D anisotropic honeycomb lattice model (J_1 - J_{ic1} model, Fig. 6), relevant for $\text{LiCrSi}_2\text{O}_6$, and estimate m for a broad range of $J_{ic1} : J_1$ ratios. For the g -factor, we adopt $g = 1.96$ from the $\chi(T)$ fits. The resulting magnetic moments are presented in the right panel of Fig. 6. In the limiting case $J_1 = 0$ ($J_{ic1} = 0$), the magnetic model becomes 0D (1D), hence the ordered moment is exactly zero.³⁶ The largest moment of $m = 2.43 \mu_B$ corresponds to the isotropic case of a regular honeycomb lattice ($J_1 = J_{ic1}$). In the wide range of $0.4 \leq J_{ic1}/J_1 \leq 2.0$ ratios, m stays nearly constant (the

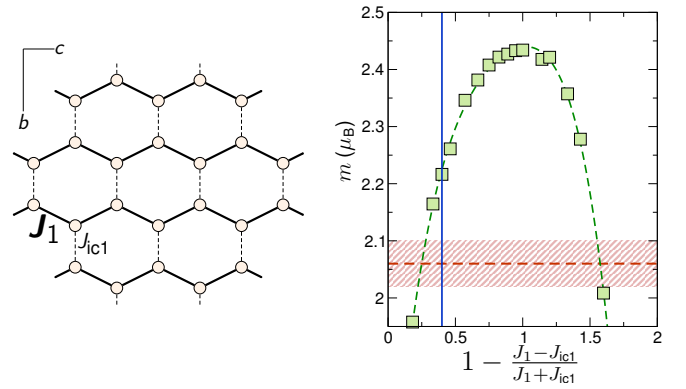


FIG. 6. (Color online) Left: anisotropic honeycomb lattice model shaped by two couplings: J_1 along the structural chains and J_{ic1} between the chains. Right: the ordered magnetic moment m in the $S = \frac{3}{2}$ anisotropic honeycomb lattice Heisenberg model for different $1 - (J_1 - J_{ic1})/(J_1 + J_{ic1})$ ratios. The m values are evaluated as $g\mu_B \langle S^z \rangle$ for $g = 1.96$. The vertical (blue) line corresponds to the $J_1 : J_{ic1} = 1 : 0.25$ solution. The horizontal (red) stripe indicates the experimental magnetic moment m_{Cr} in $\text{LiCrSi}_2\text{O}_6$ determined by neutron diffraction (Ref. 9). The dashed green curve is guide to the eye.

reduction does not exceed 3%). However, once the ratio becomes smaller than 0.4 or exceeds 2.0, the ordered moment shows a sizable reduction (Fig. 6, right panel).

Based on our fits to $\chi(T)$ and $M(H)$ data, we concluded that the magnetism of $\text{LiCrSi}_2\text{O}_6$ can be described by the J_1 - J_{ic1} model with the $1 : 0.25$ ratio of the leading couplings, depicted as the vertical line in the right panel of Fig. 6. The respective simulated magnetic moment of $\sim 2.23 \mu_B$ is significantly larger than the experimentally determined $m_{Cr} = 2.06(4) \mu_B$. Similarly, the ordered magnetic moment can be evaluated for the J_1 - J_{ic1} - J_{ic2} model realized in $\text{LiCrGe}_2\text{O}_6$. In this way, adopting $J_1 : J_{ic1} : J_{ic2} = 0.5 : 1 : 0.5$ and $g = 2.03$, we obtain $m \simeq 2.63 \mu_B$, again substantially larger than $m_{Cr} = 2.33(3) \mu_B$ determined experimentally.

Despite the overestimation of the absolute values, the difference between m for $\text{LiCrSi}_2\text{O}_6$ and $\text{LiCrGe}_2\text{O}_6$ is about $0.4 \mu_B$, which reasonably agrees with the $\sim 0.25 \mu_B$ difference found experimentally. Thus, different m_{Cr} in $\text{LiCrSi}_2\text{O}_6$ and $\text{LiCrGe}_2\text{O}_6$ originate from the different dimensionality of the underlying microscopic model, and not from magnetic frustration, as speculated earlier.

The overestimation of magnetic moments in QMC can be assigned from the partial moment transfer from Cr to the surrounding O atoms, which is neglected in the simulation. This transfer, commonly referred to as the covalency effect, was experimentally demonstrated to reduce m_{Cr} in Cr_2O_3 .³⁷ The reported reduction of $\sim 0.25 \mu_B$ is close to the difference between the experimental values of m_{Cr} in LiCrX_2O_6 and the respective QMC estimates.

The peculiar feature of pyroxenes is the inequivalence of six oxygens, surrounding the magnetic Cr atom: Four out of these six O atoms are shared by neighboring Cr atoms, hence the induced moments cancel out in the AF

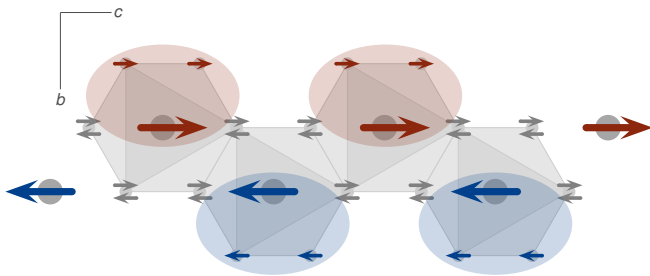


FIG. 7. (Color online) Magnetic chains of edge-sharing CrO_6 octahedra in the AF ordered state. Magnetic moments on Cr (O) atoms are depicted with large (small) arrows. For each Cr, only two neighboring O atoms carry non-zero magnetic moment. As a result, the local magnetization density is shifted along the b axis.

state (Fig. 7). The remaining two O atoms carry a non-zero moment. For instance, our GGA+ U calculations with $U_d = 3\text{ eV}$ yield small moments of $m_O \simeq 0.02\mu_B$, which is twice smaller than the value required to account for the $\sim 0.25\mu_B$ reduction of m_{Cr} . Due to the limited sensitivity of computational DFT-based schemes to low magnetic moments, we propose a direct experimental measurement of m_O . Although such small moments are beyond the resolution of standard neutron scattering techniques, they can be estimated by neutron polarimetry.³⁷

Non-zero m_O can have significant ramifications, which we did not consider so far. As can be seen in Fig. 7, the concomitant effect of the magnetic moment transfer from Cr to O is the shift of magnetization density along the b axis. Interestingly, this coincides with the direction of the maximal electric polarization.² Therefore, experimental measurement of m_O can be important for understanding the ME effect in the LiCrX_2O_6 ($X = \text{Si, Ge}$) compounds.

B. Magnetostructural correlations

The combination of the small magnetic energy scale and the rich crystal chemistry of pyroxenes is advantageous for tuning the magnetic properties. However, a directed tuning is possible only if the relevant structural parameters are identified and the respective magnetostructural correlations are known. To gain better understanding of these correlations, we evaluate the mechanisms underlying intrachain as well as interchain couplings in Cr pyroxenes.

The nearest-neighbor exchange J_1 operates between two CrO_6 octahedra sharing a common O..O edge. For the AF part of the exchange, the leading hopping is mediated by the two t_{2g} orbitals lying in the same plane with the common O..O edge: xz on one Cr and yz on the other.³⁸ Since these two orbitals are σ -overlapping, they facilitate a direct d - d hopping, thus the Cr–Cr distance $d_{(\text{Cr}-\text{Cr})}$ is the key parameter, determining the strength of magnetic exchange, as was already pointed

out in Ref. 11. It should be noted, however, that the FM contribution to J_1 also depends on the Cr–Cr distance. For instance, the leading $t_{2g} \leftrightarrow e_g$ hopping in $\text{LiCrGe}_2\text{O}_6$ is reduced by about 20% compared to the respective term in $\text{LiCrSi}_2\text{O}_6$. This is smaller than $\sim 27\%$ difference in the leading $t_1^{xz \leftrightarrow yz}$ terms, responsible for the AF exchange, hence the total exchange J_1 reduces. This perfectly agrees with larger J_1 in $\text{LiCrSi}_2\text{O}_6$ ($d_{(\text{Cr}-\text{Cr})} \simeq 3.052\text{ \AA}$) than in $\text{LiCrGe}_2\text{O}_6$ ($d_{(\text{Cr}-\text{Cr})} \simeq 3.101\text{ \AA}$), and could explain the FM exchange in $\text{NaCrGe}_2\text{O}_6$ ($d_{(\text{Cr}-\text{Cr})} \simeq 3.140\text{ \AA}$).

We turn now to the magnetic exchange between the chains. In contrast to earlier conjectures, our microscopic analysis discloses that the interchain coupling is realized by two paths involving double bridges of anionic XO_4 tetrahedra (J_{ic1} and J_{ic2}). Other interchain paths, including single bridges of the XO_4 tetrahedra, are essentially inactive.

The orbitals of Si and Ge provide minor contributions to the Cr $3d$ bands (Fig. 3), thus the Cr–O..O–Cr interaction pathways are expected to be most relevant. The nature of interacting orbitals can be understood from the crystal structure. The coupling J_{ic1} requires one of the t_{2g} orbitals (yz) that overlaps with the p orbitals of O1b and O2b. Likewise, J_{ic2} involves the hopping processes through O1a and O2a, so that the xz orbital becomes active.²⁰ Altogether, each of the J_{ic1} and J_{ic2} exchanges entails only one out of three half-filled orbitals of Cr^{3+} .

At this point, an unexpected connection to V^{4+} phosphates can be drawn, because V^{4+} features only one half-filled (magnetic) orbital. It is widely accepted that phosphorous states do not contribute to the superexchange in phosphates,^{39,40} hence the V–O..O–V interaction pathways are envisaged. Similar to pyroxenes, double bridges of the PO_4 tetrahedra are more efficient than single bridges.^{41,42} According to Ref. 39, several geometrical parameters are of crucial importance for the superexchange through these double bridges: (i) the in-plane shift of the MO_6 octahedra (shear deformation of the O_4 square shared by these polyhedra); (ii) the vertical shift of the MO_6 octahedra (normal deformation of O_4); and (iii) the rotation of PO_4 tetrahedra around the O..O edges of O_4 , parallel to the M–M line (here, we use M to denote the magnetic ion, either V^{4+} in Ref. 39 or Cr^{3+} in our case). In pyroxenes, the vertical shift is nearly absent, while the in-plane shift and the rotations of the tetrahedra can be quantified by the angles θ and ϕ , respectively.⁴³ The largest AF superexchange is expected at $\theta = 90^\circ$ and $\phi = 180^\circ$. Any deviations from this fully symmetric configuration reduce the AF exchange, with the in-plane shift ($\theta > 90^\circ$) having the most pronounced effect on the coupling.³⁹

The relevant geometrical parameters for J_{ic1} and J_{ic2} are summarized in Table III. The difference between J_{ic1} and J_{ic2} is well in line with the θ_γ values: the larger in-plane shift for J_{ic2} reduces this coupling compared to J_{ic1} . The orientation of the tetrahedra (ϕ_γ) implies an opposite trend, yet this geometrical parameter seems to

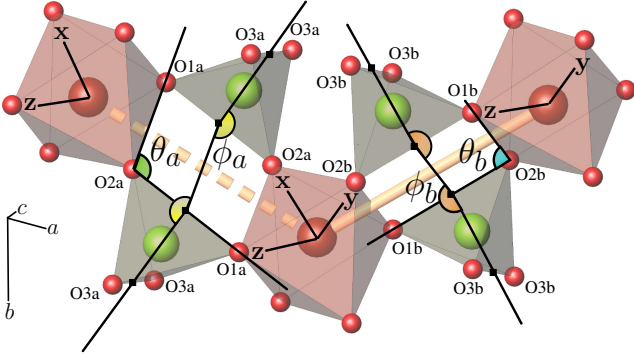


FIG. 8. (Color online) Superexchange paths facilitating the leading interchain couplings J_{ic1} (thick solid cylinder) and J_{ic2} (thick sectioned cylinder) in LiCrX_2O_6 . Similar to Fig. 2, both paths are mediated by double bridges of anionic XO_4 tetrahedra. The labels \mathbf{x} , \mathbf{y} , and \mathbf{z} denote the local coordinate axes. ϕ_a and ϕ_b angles measure the rotation of anionic tetrahedra with respect to the Cr–Cr axis. θ_a and θ_b measure the lateral shift of CrO_4 planes of the neighboring CrO_6 octahedra. Numerical values for ϕ_a , ϕ_b , θ_a , and θ_b are provided in Table III.

be of relatively low importance for the superexchange in pyroxenes, similar to the V^{4+} phosphates discussed in Ref. 39. It is worth noting that the $d_{\text{O}\cdots\text{O}}$ distance, the edge of the XO_4 tetrahedron, has no direct influence on the magnetic coupling. Both $\text{LiCrSi}_2\text{O}_6$ and $\text{LiCrGe}_2\text{O}_6$ reveal very similar interchain interactions, even though the GeO_4 tetrahedra are much bigger than their SiO_4 counterparts, and the interacting oxygen atoms ($\text{O1}\gamma$ and $\text{O2}\gamma$) are further apart. This unexpected behavior shows that the Cr–O \cdots O–Cr superexchange does not involve individual oxygen orbitals. It rather pertains to an interaction between the Cr d orbital and one of the molecular orbitals of the XO_4 tetrahedron. The interaction between $\text{O1}\gamma$ and $\text{O2}\gamma$ is largely determined by electronic interactions within the XO_4 tetrahedron, whereas the superexchange is a more subtle effect that relies on the mutual orientations of the CrO_6 octahedra and XO_4 tetrahedra.

We can also draw more general conclusions regarding microscopic aspects of magnetic pyroxenes. The replacement of Si with Ge changes the Cr–Cr distance within the chains and, consequently, the intrachain coupling J_1 , whereas the regime of the interchain couplings with $J_{ic1} > J_{ic2}$ is largely retained. The Li/Na substitution should have a stronger effect on both intrachain and interchain couplings. The size difference between Li^+ and Na^+ will further alter the Cr–Cr distance and eventually render J_1 FM.^{10,11} Additionally, Na-based pyroxenes feature a higher crystallographic symmetry ($C2/c$) that makes J_{ic1} and J_{ic2} equivalent.

TABLE III. Magnetostructural correlations for the interchain exchanges J_{ic2} and J_{ic1} . For the corresponding structural elements, see Fig. 8. $d_{\text{O}\cdots\text{O}}$ is the length (in Å) of $\text{O1}\gamma\cdots\text{O2}\gamma$ edge of the XO_4 tetrahedron. ϕ_γ is the angle (in $^\circ$) between the line connecting the midpoints of two $\text{O2}\gamma\cdots\text{O1}\gamma$ edges and the midpoint of $\text{O2}\gamma\cdots\text{O1}\gamma$ edge with that of $\text{O3}\gamma\cdots\text{O3}\gamma$ edge. θ_γ is the $\text{O1}\gamma\text{--O2}\gamma\text{--O1}\gamma$ angle (in $^\circ$). Numerical values for the exchange couplings are based on QMC simulations and GGA+ U calculations.

compound	exchange	$d_{\text{O}\cdots\text{O}}$	γ	ϕ_γ	θ_γ	
LiCrSi ₂ O ₆	$J_{\text{ic}1}$	~ 2.2 K	2.7574	a	102.3	98.9
	$J_{\text{ic}2}$	$\lesssim 1.0$ K	2.7171	b	114.3	109.2
LiCrGe ₂ O ₆	$J_{\text{ic}1}$	~ 2.3 K	2.9801	a	94.8	93.3
	$J_{\text{ic}2}$	~ 1.1 K	2.9299	b	114.2	113.2

VI. SUMMARY

Using a combination of density functional theory (DFT) calculations and quantum Monte Carlo (QMC) simulations, we evaluate the microscopic magnetic models for two $S = 3/2$ pyroxenes, $\text{LiCrSi}_2\text{O}_6$ and $\text{LiCrGe}_2\text{O}_6$. The magnetism of $\text{LiCrSi}_2\text{O}_6$ is characterized by a 2D anisotropic honeycomb lattice model, with $J_1 \simeq 8$ K running along the structural chains and J_{ic1} between the chains. Since $J_1 \gg J_{ic1}$, $\text{LiCrSi}_2\text{O}_6$ is very close to the 1D limit of this model. In contrast, the spin model of $\text{LiCrGe}_2\text{O}_6$ is 3D, with $J_1 \simeq 1.1$ K, $J_{ic1} \simeq 2.3$ K, and an additional interplane coupling $J_{ic2} \simeq 1.1$ K. Here, the strongest magnetic exchange J_{ic1} operates between the structural chains. Both spin models lack magnetic frustration, in contrast with earlier speculations.

Despite very low energies of the individual magnetic couplings in Cr^{3+} -based pyroxenes, we were able to obtain quantitative microscopic magnetic models. This would not be possible without a combination of DFT calculations and experiment, because the DFT results alone remain rather ambiguous and sensitive to the choice of the computational parameters, which are connected with the approximate treatment of the strong correlations in the $3d$ shell. The modeling of magnetic susceptibility together with the high-field magnetization data helps us to refine the model parameters and eventually explain other observable properties, such as the different ordered magnetic moment in $\text{LiCrSi}_2\text{O}_6$ and $\text{LiCrGe}_2\text{O}_6$. We believe that a similar approach can be applied to other magnetic pyroxenes, including the Fe^{3+} -based multiferroic compounds, and we hope that our work will stimulate further studies in this direction.

By comparing $\text{LiCrSi}_2\text{O}_6$ and $\text{LiCrGe}_2\text{O}_6$, we conclude that the interchain couplings in Cr^{3+} -based pyroxenes are typically AF, non-frustrated, and run via double bridges of the XO_4 tetrahedra. This is very different from the earlier assumptions of ferromagnetic interchain interactions, even though the interchain order is indeed ferromagnetic in the sense that it matches the periodicity of the crystal structure. The overall crystallographic symmetry is also

very important for the magnetism of pyroxenes.

The Li compounds with the lower $P2_1/c$ symmetry feature inequivalent interchain couplings and may even show an unexpected quasi-2D magnetism when $J_{ic1} \gg J_{ic2}$. By contrast, the higher $C2/c$ symmetry of the Na compounds should render the magnetic system 3D with possible 1D features at $J_1 \gg J_{ic1} \equiv J_{ic2}$.

ACKNOWLEDGMENTS

Fruitful discussions with D. I. Khomskii are gratefully acknowledged. OJ was supported by the Mobilitas program of the ESF, grant number MJD447, and the PUT210 grant of the Estonian Research Council. AT was supported via the ESF Mobilitas program, grant number MTT77. Discussions with Martin Rotter are kindly acknowledged. We also acknowledge the support of the HLD at HZDR, member of the European Magnetic Field Laboratory (EMFL).

-
- * janson@cpfs.mpg.de
- ¹ See, e.g., H. Katsura, N. Nagaosa, and A. V. Balatsky, *Phys. Rev. Lett.* **95**, 057205 (2005), [cond-mat/0412319](#); L. C. Chapon, P. G. Radaelli, G. R. Blake, S. Park, and S.-W. Cheong, *Phys. Rev. Lett.* **96**, 097601 (2006); H. Kimura, Y. Kamada, Y. Noda, K. Kaneko, N. Metoki, and K. Kohn, *J. Phys. Soc. Jpn.* **75**, 113701 (2006); Y. J. Choi, H. T. Yi, S. Lee, Q. Huang, V. Kiryukhin, and S.-W. Cheong, *Phys. Rev. Lett.* **100**, 047601 (2008).
 - ² S. Jodlauk, P. Becker, J. A. Mydosh, D. I. Khomskii, T. Lorenz, S. V. Streltsov, D. C. Hezel, and L. Bohatý, *J. Phys.: Condens. Matter* **19**, 432201 (2007), [arXiv:0709.1125](#).
 - ³ I. Kim, B.-G. Jeon, D. Patil, S. Patil, G. Nénert, and K. H. Kim, *J. Phys.: Condens. Matter* **24**, 306001 (2012).
 - ⁴ G. Nénert, I. Kim, M. Isobe, C. Ritter, A. N. Vasiliev, K. H. Kim, and Y. Ueda, *Phys. Rev. B* **81**, 184408 (2010).
 - ⁵ Y. Sasago, M. Hase, K. Uchinokura, M. Tokunaga, and N. Miura, *Phys. Rev. B* **52**, 3533 (1995).
 - ⁶ M. Isobe, E. Ninomiya, A. N. Vasil'ev, and Y. Ueda, *J. Phys. Soc. Jpn.* **71**, 1423 (2002).
 - ⁷ S. J. Blundell, C. A. Steer, F. L. Pratt, I. M. Marshall, W. Hayes, and R. C. C. Ward, *Phys. Rev. B* **67**, 224411 (2003) and references therein.
 - ⁸ B. Pedrini, S. Wessel, J. L. Gavilano, H. R. Ott, S. M. Kazakov, and J. Karpinski, *Eur. Phys. J. B* **55**, 219 (2007), [cond-mat/0606150](#) and references therein.
 - ⁹ G. Nénert, M. Isobe, C. Ritter, O. Isnard, A. N. Vasiliev, and Y. Ueda, *Phys. Rev. B* **79**, 064416 (2009).
 - ¹⁰ G. Nénert, C. Ritter, M. Isobe, O. Isnard, A. N. Vasiliev, and Y. Ueda, *Phys. Rev. B* **80**, 024402 (2009).
 - ¹¹ S. V. Streltsov and D. I. Khomskii, *Phys. Rev. B* **77**, 064405 (2008), [arXiv:0710.5351](#).
 - ¹² A. A. Tsirlin, B. Schmidt, Y. Skourski, R. Nath, C. Geibel, and H. Rosner, *Phys. Rev. B* **80**, 132407 (2009), [arXiv:0907.0391](#).
 - ¹³ K. Koepnik and H. Eschrig, *Phys. Rev. B* **59**, 1743 (1999).
 - ¹⁴ G. Kresse and J. Furthmüller, *Phys. Rev. B* **54**, 11169 (1996); *Comput. Mater. Sci.* **6**, 15 (1996).
 - ¹⁵ J. P. Perdew and Y. Wang, *Phys. Rev. B* **45**, 13244 (1992).
 - ¹⁶ J. P. Perdew, K. Burke, and M. Ernzerhof, *Phys. Rev. Lett.* **77**, 3865 (1996).
 - ¹⁷ C. Adamo and V. Barone, *J. Chem. Phys.* **110**, 6158 (1999).
 - ¹⁸ J. Heyd, G. E. Scuseria, and M. Ernzerhof, *J. Chem. Phys.* **118**, 8207 (2003); *J. Chem. Phys.* **124**, 219906 (2006).
 - ¹⁹ O. Janson, S. Chen, A. A. Tsirlin, S. Hoffmann, J. Sichelschmidt, Q. Huang, Z.-J. Zhang, M.-B. Tang, J.-T. Zhao, R. Kniep, and H. Rosner, *Phys. Rev. B* **87**, 064417 (2013), [arXiv:1211.1260](#).
 - ²⁰ See Supplementary information for hopping matrix elements t_{ij} evaluated using Wannier functions.
 - ²¹ H. Eschrig and K. Koepnik, *Phys. Rev. B* **80**, 104503 (2009), [arXiv:0905.4844](#).
 - ²² S. Todo and K. Kato, *Phys. Rev. Lett.* **87**, 047203 (2001), [cond-mat/9911047](#).
 - ²³ A. W. Sandvik, *Phys. Rev. B* **59**, R14157 (1999), [cond-mat/9902226](#).
 - ²⁴ B. Bauer, L. D. Carr, H. G. Evertz, A. Feiguin, J. Freire, S. Fuchs, L. Gamper, J. Gukelberger, E. Gull, S. Guertler, A. Hehn, R. Igarashi, S. V. Isakov, D. Koop, P. N. Ma, P. Mates, H. Matsuo, O. Parcollet, G. Pawłowski, J. D. Picon, L. Pollet, E. Santos, V. W. Scarola, U. Schollwöck, C. Silva, B. Surer, S. Todo, S. Trebst, M. Troyer, M. L. Wall, P. Werner, and S. Wessel, *J. Stat. Mech.* **2011**, P05001 (2011), [arXiv:1101.2646](#); A. Albuquerque, F. Alet, P. Corboz, P. Dayal, A. Feiguin, S. Fuchs, L. Gamper, E. Gull, S. Gürtler, A. Honecker, R. Igarashi, M. Körner, A. Kozhevnikov, A. Läuchli, S. R. Manmana, M. Matsumoto, I. P. McCulloch, F. Michel, R. M. Noack, G. Pawłowski, L. Pollet, T. Pruschke, U. Schollwöck, S. Todo, S. Trebst, M. Troyer, P. Werner, and S. Wessel, *J. Magn. Magn. Mater.* **310**, 1187 (2007), [arXiv:0801.1765](#).
 - ²⁵ G. J. Redhammer and G. Roth, *Z. Kristallogr.* **219**, 585 (2004).
 - ²⁶ G. J. Redhammer, G. Roth, and G. Amthauer, *Acta Crystallogr. C* **64**, i97 (2008).
 - ²⁷ Y. Matsushita, F. Izumi, M. Isobe, and Y. Ueda, *Solid State Sci.* **12**, 676 (2010).
 - ²⁸ I. I. Mazin, *Phys. Rev. B* **75**, 094407 (2007), [cond-mat/0701520](#).
 - ²⁹ For example, S. P. Ong, V. L. Chevrier, and G. Ceder, *Phys. Rev. B* **83**, 075112 (2011); F. Iori, M. Gatti, and A. Rubio, *Phys. Rev. B* **85**, 115129 (2012), [arXiv:1201.3308](#); H. Chen and J. H. Harding, *Phys. Rev. B* **85**, 115127 (2012).
 - ³⁰ X. Rocquefelte, K. Schwarz, and P. Blaha, *Sci. Rep.* **2**, 759 (2012).
 - ³¹ J. P. Perdew, M. Ernzerhof, and K. Burke, *J. Chem. Phys.* **105**, 9982 (1997).
 - ³² J. Paier, M. Marsman, K. Hummer, G. Kresse, I. C. Gerber, and J. G. Ángyán, *J. Chem. Phys.* **124**, 154709 (2006).

- ³³ For an instructive example, see S. Lebernegg, A. A. Tsirlin, O. Janson, R. Nath, J. Sichelschmidt, Y. Skourski, G. Amthauer, and H. Rosner, *Phys. Rev. B* **84**, 174436 (2011), [arXiv:1107.0250](#).
- ³⁴ The peculiar experimental setup of a pulsed-field measurement does not allow to determine the absolute magnetization: the signal picked up by the coil comes from a certain part of the sample, only. Unfortunately, the ratio between the exposed and unexposed material is unknown. Our attempts to scale the data using the low-field magnetization measurements failed for $\text{LiCrSi}_2\text{O}_6$, thus we converted the measured signal into the respective fraction of the saturation magnetization amounting to gS (Fig. 5).
- ³⁵ A. W. Sandvik, *Phys. Rev. B* **56**, 11678 (1997), [cond-mat/9707123](#).
- ³⁶ P. W. Anderson, *Phys. Rev.* **86**, 694 (1952).
- ³⁷ P. J. Brown, J. B. Forsyth, and F. Tasset, *Proc. R. Soc. London, Ser. A* **442**, 147 (1993).
- ³⁸ Different orbital characters ensue from the peculiar symmetry of LiCrX_2O_6 . Here, we adopt local coordinate frame with the x and y axes running towards the O2a and O2b atoms. This leads to different frames on the neighboring Cr atoms: the x axis on one Cr transforms into the $-y$ axis on the neighboring Cr, the y transforms into the $-x$, while z changes its sign.
- ³⁹ M. Roca, P. Amorós, J. Cano, M. D. Marcos, J. Alamo, A. Beltrán-Porter, and D. Beltrán-Porter, *Inorg. Chem.* **37**, 3167 (1998).
- ⁴⁰ O. Janson, A. A. Tsirlin, J. Sichelschmidt, Y. Skourski, F. Weickert, and H. Rosner, *Phys. Rev. B* **83**, 094435 (2011), [arXiv:1011.5393](#).
- ⁴¹ S. Petit, S. A. Borshch, and V. Robert, *J. Solid State Chem.* **170**, 237 (2003).
- ⁴² A. A. Tsirlin, R. Nath, J. Sichelschmidt, Y. Skourski, C. Geibel, and H. Rosner, *Phys. Rev. B* **83**, 144412 (2011), [arXiv:1101.2546](#).
- ⁴³ The angle ϕ_γ is measured between the line connecting the midpoints of two $\text{O}2_\gamma\text{--O}1_\gamma$ edges and the midpoint of $\text{O}2_\gamma\text{--O}1_\gamma$ edge with that of $\text{O}3_\gamma\text{--O}3_\gamma$ edge (Fig. 8), where $\gamma = a$ or b .

Supplementary information for
Magnetic pyroxenes $\text{LiCrGe}_2\text{O}_6$ and $\text{LiCrSi}_2\text{O}_6$:
dimensionality crossover in a non-frustrated $S = \frac{3}{2}$ Heisenberg model

O. Janson, G. Nénert, M. Isobe, Y. Skourski, Y. Ueda, H. Rosner, and A. A. Tsirlin

TABLE S1. Leading transfer integrals $t_i^{mm'}$ (m and m' are orbital indices) in $\text{LiCrSi}_2\text{O}_6$ and $\text{LiCrGe}_2\text{O}_6$, evaluated by mapping the GGA band structure onto the Wannier basis. All values are given in meV. The coordinate systems are local (Cr-centered), with the x and y axes running towards the neighboring O2a and O2b atoms, respectively (see Fig. S1, (a)). The leading terms are shown bold. Color denotes whether the respective term contributes to **antiferromagnetic** or **ferromagnetic** exchange. Note that for t_1 , the hopping matrix is not symmetric ($t_1^{mm'} \neq t_1^{m'm}$) due to the absence of centre of inversion between the respective Cr atoms. In contrast, both interchain paths pass through the center of inversion, thus $t_{ij}^{mm'} = \pm t_{ij}^{m'm}$.

LiCrSi ₂ O ₆						LiCrGe ₂ O ₆					
t_1 ($d_{\text{Cr-Cr}} = 3.052 \text{ \AA}$)						t_1 ($d_{\text{Cr-Cr}} = 3.101 \text{ \AA}$)					
	$ xy\rangle$	$ xz\rangle$	$ yz\rangle$	$ z^2 - r^2\rangle$	$ x^2 - y^2\rangle$		$ xy\rangle$	$ xz\rangle$	$ yz\rangle$	$ z^2 - r^2\rangle$	$ x^2 - y^2\rangle$
$\langle xy $	-50	-18	54	-	-12	$\langle xy $	-37	-26	66	-18	-
$\langle xz $	-60	-15	53	-	-15	$\langle xz $	-59	-25	45	12	-23
$\langle yz $	19	135	-	-90	-140	$\langle yz $	13	98	-16	-108	-115
$\langle z^2 - r^2 $	32	100	-	24	-59	$\langle z^2 - r^2 $	62	73	10	69	-89
$\langle x^2 - y^2 $	-	-116	12	43	-	$\langle x^2 - y^2 $	-	-108	31	83	10
t_{ic1} ($d_{\text{Cr-Cr}} = 5.336 \text{ \AA}$)						t_{ic1} ($d_{\text{Cr-Cr}} = 5.581 \text{ \AA}$)					
	$ xy\rangle$	$ xz\rangle$	$ yz\rangle$	$ z^2 - r^2\rangle$	$ x^2 - y^2\rangle$		$ xy\rangle$	$ xz\rangle$	$ yz\rangle$	$ z^2 - r^2\rangle$	$ x^2 - y^2\rangle$
$\langle xy $	-	11	-12	-	-	$\langle xy $	-	-	-	31	-
$\langle xz $	-11	-	-	-	-12	$\langle xz $	-	-	-10	-	-
$\langle yz $	-12	-	62	-26	-53	$\langle yz $	-	10	67	-17	-66
$\langle z^2 - r^2 $	-	-	26	68	59	$\langle z^2 - r^2 $	-31	-	17	121	85
$\langle x^2 - y^2 $	-	-12	53	59	-	$\langle x^2 - y^2 $	-	-	66	85	-14
t_{ic2} ($d_{\text{Cr-Cr}} = 5.322 \text{ \AA}$)						t_{ic2} ($d_{\text{Cr-Cr}} = 5.464 \text{ \AA}$)					
	$ xy\rangle$	$ xz\rangle$	$ yz\rangle$	$ z^2 - r^2\rangle$	$ x^2 - y^2\rangle$		$ xy\rangle$	$ xz\rangle$	$ yz\rangle$	$ z^2 - r^2\rangle$	$ x^2 - y^2\rangle$
$\langle xy $	-	-13	19	-18	-	$\langle xy $	-	-	11	-13	-
$\langle xz $	13	-52	-	32	-42	$\langle xz $	-	-66	-	47	-78
$\langle yz $	19	-	-	-	-10	$\langle yz $	11	-	-	-	-
$\langle z^2 - r^2 $	18	32	-	44	-40	$\langle z^2 - r^2 $	13	47	-	74	-66
$\langle x^2 - y^2 $	-	-42	10	-40	-	$\langle x^2 - y^2 $	-	-78	-	-66	-

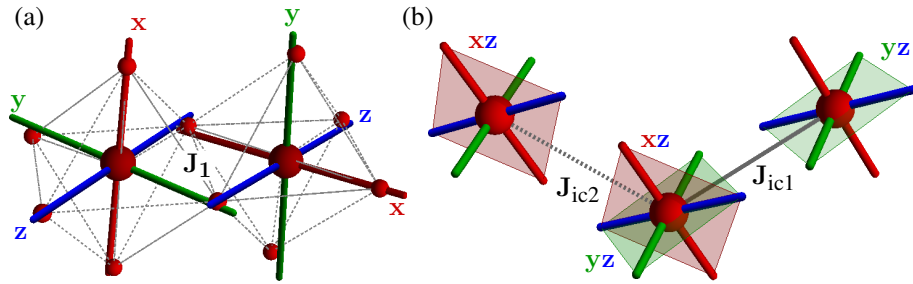


FIG. S1. Local coordinate systems of CrO_6 tetrahedra used for construction of the Wannier functions. (a) The antiferromagnetic part of nearest-neighbor exchange J_1 is dominated by the direct overlap of xz and yz orbitals. (b) The antiferromagnetic exchange between the chains is ruled by the superexchange between nearly in-plane $yz(xz)$ orbitals for the J_{ic1} (J_{ic2}) coupling.